

Enhancement of neutral beam deposition in hydrogen discharge using carbon pellet injection in LHD

Katsunori IKEDA, Masaki OSAKABE, Allan WHITEFORD¹⁾, Kenichi NAGAOKA, Mikiro YOSHINUMA, Katsumi IDA, Osamu KANEKO, Daiji KATO, Shigeru MORITA, Haruhisa NAKANO, Yasuhiko TAKEIRI, Katsuyoshi TSUMORI, and LHD experiment group

National Institute for Fusion Science, Toki, Gifu 509-5292, Japan

¹⁾*University of Strathclyde, 107 Rottenrow Glasgow, UK*

(Received: 20 November 2009 / Accepted: 26 February 2010)

The central ion temperature in the large helical device (LHD), as measured by charge-exchange recombination spectroscopy, has been improved to a record 5.6 keV by combining 21 MW of neutral beam heating with the injection of a carbon pellet. The intensity of the neutral beam emission of the hydrogen Balmer line ($H\alpha : n = 3 \rightarrow 2$) was observed to weaken along the beam injection axis following the carbon pellet injection due to the increased beam attenuation. The beam-emission intensity was reconstructed by calculating the density distribution, and the beam-stopping coefficients, along a beam injection axis and was found to fit well to the measured beam-emission for a mixed hydrogen and carbon target plasma. The dynamics of the neutral beam deposition power and the carbon fraction were estimated from the beam-emission measurements using data from ADAS. We conclude that the beam deposition power in a carbon pellet discharge is enhanced over that of a pure hydrogen discharge.

Keywords: NBI, neutral beam emission, beam attenuation, ADAS, LHD

1. Introduction

In many magnetically confined fusion devices, neutral beam injectors (NBIs) are widely used to produce high performance plasmas [1–5]. In future devices, such as the International Thermonuclear Experimental Reactor (ITER), it is anticipated to heat the plasma with neutral beams which perform at higher energies than most current systems [6]. The higher energy beams will be based on negative ion sources.

In the large helical device (LHD), we have a low energy perpendicular NBI (BL4) and three high-energy tangential NBIs (BL1, BL2, and BL3), as shown in Fig. 1. In particular, two tangential beam lines (BL1 and BL2) with the hydrogen negative-ion sources have operated continuously for over ten years [5]. One 180 keV tangential neutral beam passes through the plasma and impacts carbon armor tiles on the inner surface of the LHD vacuum vessel. We measure the beam deposition power with a thermocouple placed on the beam armor tiles, and the measured beam deposition efficiency is calculated by averaging over a single discharge [7].

In a recent LHD experiment, with four neutral beam injectors and the injection of a carbon pellet, the central ion temperature was found to be significantly higher than in NBI-only heated discharges. The beam deposition in this discharge was investigated by observing the hydrogen Balmer emission ($H\alpha : n = 3 \rightarrow 2$) from one of the injected neutral beams.

In this article we present the dynamics of beam-

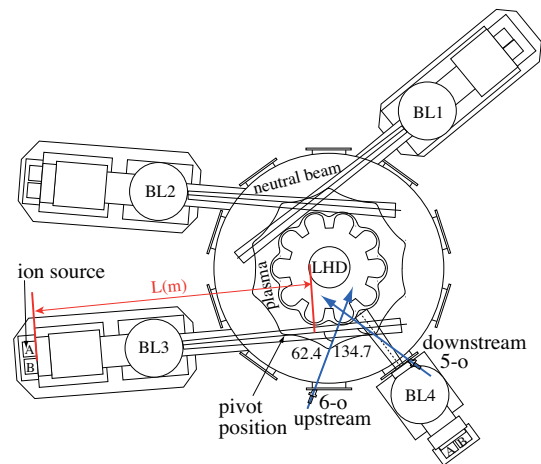


Fig. 1 Schematic view of LHD equipped with three tangential NBIs and a perpendicular NBI. Two optical sight lines set along the BL3 injector allow observation of the $H\alpha$ spectrum of the beam-emission. BL3 has two ion sources (3A and 3B), the beams extracted from the 3A (beam-3A) and the 3B (beam-3B) are tilted small angles from the beam line axis to pass through the beam injection port. L is the distance from the ion source.

emission evolution in a NBI/carbon pellet heated discharge. We calculate the beam-emission intensity using the beam stopping coefficients and the target-plasma density along the beam injection axis. Finally, we discuss the beam deposition power and the carbon fraction in a high ion-temperature discharge.

author's e-mail: ikeda.katsunori@lhd.nifs.ac.jp

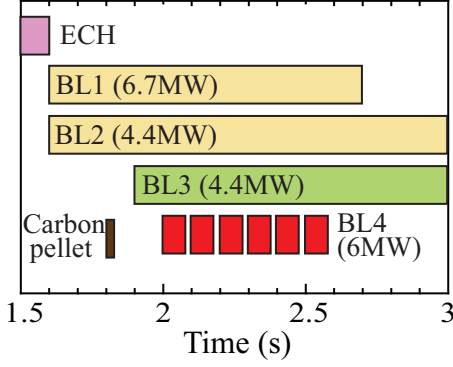


Fig. 2 Time sequence of a carbon pellet discharge heated by electron cyclotron heating and four NBIs. BL4 is also used with CXRS to obtain the ion temperature profile.

2. Beam-emission Measurement

Figure 1 shows the arrangement of two sight lines through an outer port of LHD that are used for beam-emission measurements. The upstream sight line and the downstream sight line are tilted at 62.4° and 134.7° respectively with respect to the beam injection axis of the third beam line (BL3) [8]. Each neutral beam forms Gaussian distribution in horizontal, and the standard deviation σ is 12 cm at the armor position in a typical operation. The divergence angle of the single beamlet is less than 10 mrad. The neutral beam becomes maximum strength on the beam axis. Since beam emission intensity is proportional to the product of the residual beam density and the electron density of the target plasma, the beam emission signal also becomes maximum intensity at the position of beam center. About 70% of the beam emission signal is generated from the 2σ area around the beam center. Optical emission from the neutral beams and the plasma discharge are corrected by a small lens, and transferred by a quartz optical fiber to a 25 cm Czerny-Turner spectrometer with a grating of 1800 grooves/mm. The spectrometric system was calibrated using an Urbright sphere with a standard lamp.

The wavelength of the beam-emission $H\alpha$ spectrum is shifted in the observed spectrum due to the Doppler effect induced by the beam speed and the observation angle. Hence, we can observe the beam-emission $H\alpha$ spectrum separated from the dominant $H\alpha$ emission (656.3 nm) emitted from the background plasma. The weak beam-emission signals are detected using an intensified charge-coupled device (ICCD) detector cooled to -20°C which is positioned at the focal plane of the spectrometer. We can simultaneously acquire the beam-emission spectrum of both the upstream and the downstream positions because the spectra shift in opposite directions.

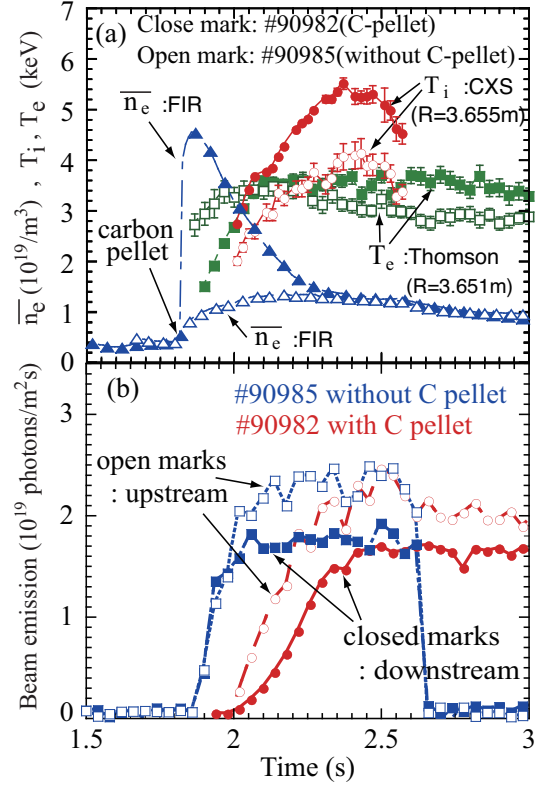


Fig. 3 (a) Dynamics of the averaged electron density \bar{n}_e , the electron temperature and the ion temperature in the carbon pellet discharge of shot 90982. The waveforms in discharge 90985 without a carbon pellet is also plotted. (b) Dynamics of the intensity of the beam-emission $H\alpha$ spectrum at the upstream and downstream positions. Circles and squares give the beam-emission intensity in the discharge 90982 and 90985, respectively. The open symbols are measured at the upstream position, and the solid symbols are measured at the downstream position.

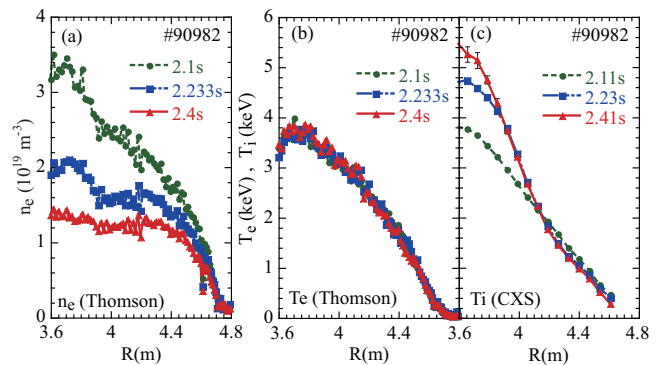


Fig. 4 Outer half radial profiles of electron density (a), electron temperature (b), and ion temperature (c) for the LHD sequence time $t = 2.1$ s, $t = 2.23$ s, and $t = 2.4$ s in the carbon pellet discharge.

3. High-Temperature Discharge using Carbon Pellet Injection

Figure 2 shows the sequence of events for the carbon pellet discharge in LHD shot number 90982. The

magnetic field axis is 3.6 m long and the magnetic field strength is 2.9 T. The plasma is initiated by electron-cyclotron heating, which is then sustained by two tangential NBIs (BL1 and BL2), giving a low line-averaged electron densities of $\bar{n}_e = 0.4 \times 10^{19} \text{ m}^{-3}$, as measured by a far-infrared laser interferometer (see Fig. 3(a)). A small carbon pellet, with a diameter of 1.4 mm, was injected into the plasma at $t = 1.8$ s causing the electron density to increase rapidly as much as an order of magnitude. Additional tangential NBI heating (BL3) was introduced 100 ms after the carbon pellet injection : this system was used for measurements of the beam-emission. Just over 100 ms later the low-energy NBI heating (BL4) was started to further increase the ion heating : this system is used for the charge-exchange recombination spectroscopy (CXRS) to measure the ion temperature profile.

At $t = 2.4$ s, the electron density decreased to $\bar{n}_e = 1.3 \times 10^{19} \text{ m}^{-3}$ and the ion temperature increased to $T_i = 5.6$ keV. In a similar discharge in hydrogen, without the carbon pellet injection (shot number 90985), the electron density built up smoothly as a result of the NBI injection. The electron density of this pellet-free discharge reached the same density as that for the carbon pellet discharge at $t = 2.4$ s. The central ion temperature in pellet-free discharge is 4.1 keV, which is slightly higher than the electron temperature measured with a Thomson-scattering system.

The beam-emission intensities in the discharge with and without carbon pellet are plotted in Fig. 3(b). We clearly observed the beam-emission spectrum at both upstream and downstream positions at the beginning of the beam injection in the pellet-free discharge of shot 90985. However, for the carbon pellet discharge 90982, the beam-emission at both the observation positions was not seen in the 100 ms following the BL3 beam injection. We posit that strong beam attenuation occurs during this period of beam injection in the carbon pellet discharge. The beam-emission intensity does increase with time after $t = 1.9$ s and we suggest that the beam particle penetration increases then because beam-emission intensity is proportional to the residual beam density. After $t = 2.4$ s both discharges exhibit almost the same beam-emission, and the ion temperature is maintained at 5 keV in the carbon pellet discharge.

4. Estimating the Neutral Beam Attenuation and Carbon Fraction

Figure 4 shows the profiles of the electron density n_e , the electron temperature T_e , and the ion temperature T_i for the outer half of LHD at three times following carbon pellet injection. The electron density profile is measured by Thomson scattering and forms a peak at $t = 2.1$ s after carbon pellet injection, as shown in Fig. 4(a). The central electron density

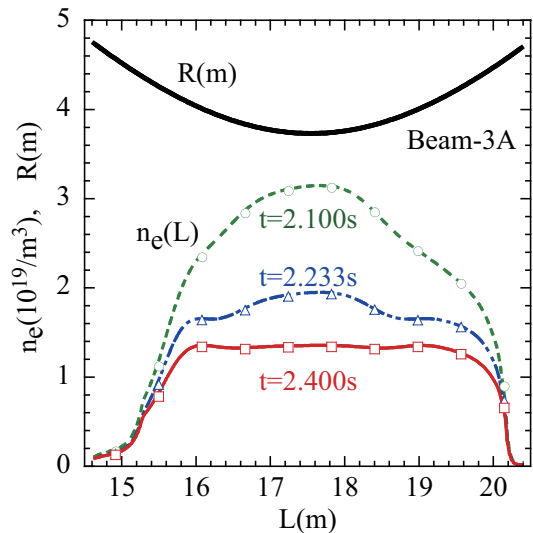


Fig. 5 Electron density distribution of the target plasma along the beam injection axis for the LHD sequence time $t = 2.1$ s (circles), $t = 2.23$ s (triangles) and $t = 2.4$ s (squares). The bold line is the major radius R from LHD center.

decreases to $n_e = 1.3 \times 10^{19} \text{ m}^{-3}$ with a flat profile at $t = 2.4$ s. The electron temperature profiles vary little over this period, with a central temperature of $T_e = 3.8$ keV, as shown in Fig. 4(b). At $t = 2.1$ s, when the density distribution is peaked, the ion temperature distribution adopts the same shape as the T_e distribution, and the central T_i grows to 5.6 keV until $t = 2.4$ s, as shown in Fig. 4(c). Understanding of the dynamics of the ion heating power is required to explain the increase in ion temperature.

If the radial density distributions along the beam injection axis is known, we can estimate the beam attenuation. The intensity of the $H\alpha$ beam-emission is proportional to the electron density, the beam density, and the beam-emission coefficient [9]. In our experimental configuration, the local beam-emission flux $\Phi(L)$ at the position L along the beam injection axis is expressed as

$$\Phi(L) \propto n_e(L)\epsilon_{cr}(L)N_b(L), \quad (1)$$

where $n_e(L)$, $\epsilon_{cr}(L)$, and $N_b(L)$ are the local electron density, the emission coefficient, and the neutral beam density, respectively, at the point L . In the present work, we used beam-stopping coefficient, S_{cr} , from the Atomic Data and Analysis Structure (ADAS) database [10–12]. The local beam density $N_b(L)$ is given by the exponential function

$$N_b(L) = N_b(P)\exp\left(-\int_P^L n_e(l)S_{cr}(l)\sqrt{\frac{m}{2E}}dl\right), \quad (2)$$

where the $N_b(P)$ is the neutral beam density path through the beam injection port at port position P , $n_e(l)$ is the local electron density, $S_{cr}(l)$ is the local

stopping coefficient, m is the mass of the beam particles, and E is the beam energy. In addition, we define the beam attenuation factor $\eta = N_b(L)/N_b(P)$.

The neutral beam passes through the plasma, with a path length through plasma of nearly 5m. Figure 5 shows the major radius of LHD and the electron density distribution, for the three times of Fig. 4, along the beam injection path where the horizontal axis L is the distance from the BL3 ion source. At $L = 17.5$ m along the beam path it comes closest to the center of LHD. The electron densities of the target plasma reach a maximum near this closest point at $t = 2.1$ s and at $t = 2.233$ s. At $t = 2.4$ s, the target plasma density is almost constant along the beam injection path.

Figure 6(a) shows the reconstructed beam-emission intensities at both the upstream and downstream positions. In this analysis, we have added the beam-emission intensities at two positions on the beam center of two beams (beam-3A and beam-3B), since the beam-emission is maximum intensity at the beam center due to its Gaussian profile. If we assume a pure hydrogen discharge for shot 90982 (recall it has a carbon pellet injection) strong beam-emission appears at $t = 2.1$ s in the calculated beam-emission due to the increase in penetration of the beam particles, as shown by the narrow lines in Fig. 6(a). However as these calculated intensities are not consistent with the measurements, we need adopt a mixed hydrogen and carbon model for the target plasma. The carbon fraction is defined as $n_C/(n_H + n_C)$, where n_C and n_H is the carbon density and the hydrogen density, respectively. Figures 6(b) and 6(c) show the reconstructed beam-emission intensities obtained by assuming a fixed carbon fraction at both the upstream and downstream positions, respectively. With an increasing carbon fraction, the beam-emission intensity decreases at both positions due to greater beam attenuation. For a 20% carbon fraction, the beam-emission intensity decreases by 30% over that for a pure hydrogen discharge in the upstream position at $t = 2.1$ s. We expect the signal strength to be unobservable at the downstream position with this carbon fraction. From this result, we can estimate the dynamics of the carbon fraction, which are shown by the cross marks in Fig. 7. we find that the plasma is composed of about 28% carbon particles at $t = 2.03$ s, which decreases to 0.5% at $t = 2.4$ s when the maximum T_i is achieved. As shown in Fig. 3(a), the electron density rapidly increases by as much as an order of magnitude after the carbon pellet injection. If the carbon particles fully ionize, the plasma carbon fraction increases to approximately 60%. Thus, the carbon density decreases faster than the electron density while T_i rises. From this analysis, the reconstructed beam-emission intensities, calculated in a mixed hydrogen-

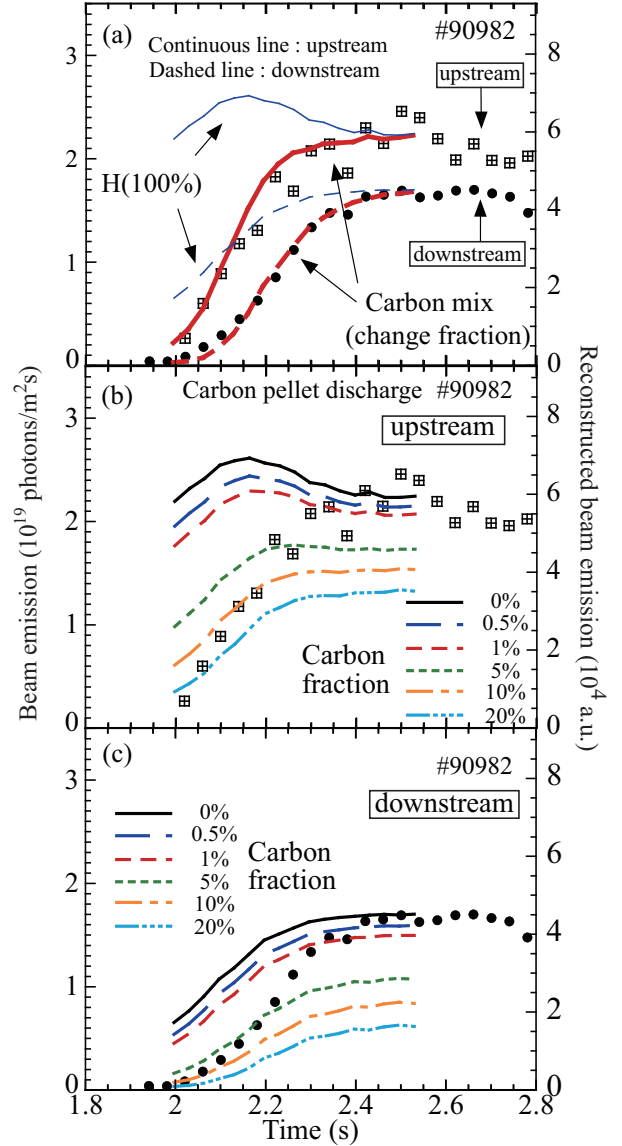


Fig. 6 (a) Thin lines show the reconstructed beam-emission intensities calculated with ADAS coefficients and under the assumption of a pure hydrogen plasma with the same density profile as shot 90982. Bold lines are the result of fitting the reconstructed beam-emission intensities for the mixed hydrogen and carbon plasma. Continuous lines and dashed lines give the estimated values at the upstream and downstream positions, respectively. Squares and circles give the measured value at the upstream and downstream position, respectively. Panels (b) and (c) show the reconstructed beam-emission intensities calculated from the constant carbon fraction at the upstream and downstream positions, respectively.

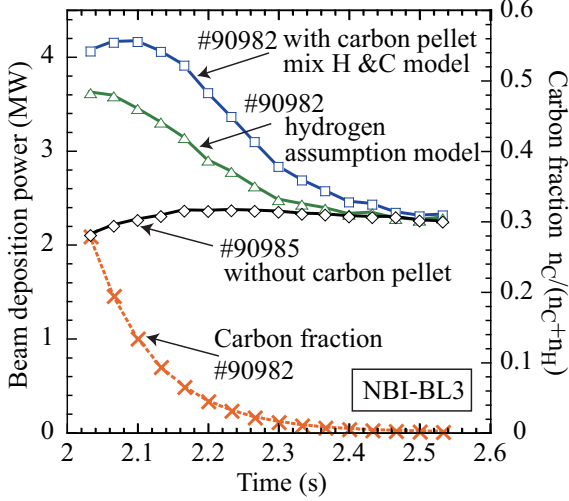


Fig. 7 Crosses show the estimated carbon fraction $n_C/(n_H + n_C)$ in the carbon pellet discharge. Squares show the beam deposition power estimated by beam-emission measurement using the mixed hydrogen-carbon target model in the carbon pellet discharge 90982. The data shown by the triangles are based on assuming a pure hydrogen target model in 90982. Diamonds show the beam deposition power for shot 90985 with no carbon pellet, estimated from the beam-emission measurement.

carbon model for both the upstream and downstream position, fit well to the measured beam-emission intensities (see bold lines in Fig. 6(a)).

Figure 8 shows the beam attenuation factors η along the beam injection axis at the time $t = 2.1$ s, $t = 2.23$ s, and $t = 2.4$ s. Because the target plasma discharge contains 13% carbon impurities at $t = 2.1$ s, 80% of the neutral beam particles are deposited before the point of closest approach to the center at $L = 17.5$ m, and 97% of the neutral beam particles injected are deposited into the plasma. At $t = 2.4$ s, when the density distribution is flat with a 0.5% carbon impurities, the beam deposition rate is reduced to 55%. Here, we have estimated the evolution of the beam deposition power (P_{dep}), defined as $P_{dep} = (1 - \eta) \times P_{inp}$, where P_{inp} is the input beam power passing through the beam injection port.

The square symbols in Fig. 7 show the beam deposition power estimated from the beam-emission measurement of the carbon pellet discharge of shot 90982. The maximum deposited power is 4.2 MW at $t = 2.1$ s which decreases to 2.4 MW at $t = 2.4$ s, which is almost the same deposition power as for the pellet-free discharge of the shot 90985 (diamond symbols). Compared with a pellet-free discharge, the neutral-beam heating power improves about 2 MW due to the injection of a carbon pellet at the beginning of the BL3 beam injection. The triangle symbols in Fig. 7 show the beam deposition power assuming

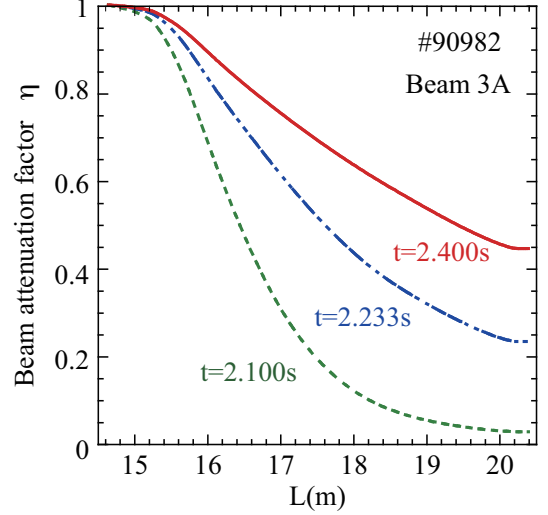


Fig. 8 Beam attenuation factors η along the beam injection axis at the LHD sequence times $t = 2.1$ s, $t = 2.23$ s, and $t = 2.4$ s, plotted as the dashed line, the chain double-dashed line, and the solid line, respectively, in the carbon pellet discharge.

hydrogen-only discharge after carbon pellet injection. The difference in the deposited beam power between pure hydrogen discharge and discharge with 13% carbon with the same density profile at $t = 2.1$ s is 0.8 MW, which we believe is the net effect of carbon in this discharge.

In conclusion, the central ion temperature has been improved to 5.6 keV by combining 21 MW of NBI heating with a carbon pellet injection. Strong beam attenuation is observed with beam-emission H α spectroscopy and the carbon fraction and beam deposition power have been estimated by comparing the beam-emission with an ADAS calculation. The beam deposition power for carbon pellet discharge is enhanced by the carbon pellet until the ion temperature saturates. The method of diagnosing beam attenuation using the beam-emission has been shown to be useful for understanding the dynamics of the beam deposition power.

ACKNOWLEDGMENTS

The authors thank the LHD and NBI staff for their operational and diagnostic support. We also thank Professor I. Murakami (National Institute for Fusion Science) and Professor H. Summers and Dr. M. O'Mullane (University of Strathclyde) for useful discussions. This work is supported by the budget for NIFS09ULBB517.

References

- [1] M. Kuriyama, N. Akino, N. Ebisawa, *et al.*, Journal of Nuclear Science and Technology **35** (11) 739 (1998).
- [2] R. King, C. Challis, D. Ciric, Fusion Engineering and Design **74** 455 (2005).
- [3] J.L. Luxon, Nucl. Fusion **42** 614 (2002).
- [4] E. Speth Plasma Science and Technology **6** (1) 2135 (2004).
- [5] Y. Takeiri, O. Kaneko, K. Tsumori *et al.*, Nucl. Fusion **46** S199 (2006).
- [6] R. S. Hemsworth, A. Tanga and V. Antoni, Rev. Sci. Instrum. **79**, 02C109 (2008).
- [7] M. Osakabe, Y. Takeiri, K. Tsumori *et al.*, Rev. Sci. Instrum. **72** 590 (2001).
- [8] K. Ikeda, M. Osakabe, A. Whiteford *et al.*, Transactions of Fusion Science and Technology **51** (2T), 283-285, (2007).
- [9] W. Mandl, R. C. Wolf, M. G. von Hellermann and H. P. Summers, Plasma Phys. Control. Fusion **35** 1373 (1993).
- [10] H. Anderson, M. G. von Hellermann, R. Hoekstra *et al.*, Plasma Phys. Control. Fusion **42** 781 (2000).
- [11] H. P. Summers, W. J. Dickson, M. G. O'Mullane *et al.*, Plasma Phys. Control. Fusion **48** 263 (2006).
- [12] H. P. Summers, H. Anderson, T. Kato and S. Murakami, Research Report NIFS-DATA Series No. 55, Nagoya, November (1999).